# Electrochemically Driven C-N Bond Formation from $CO_2$ and Ammonia at the Triple-Phase Boundary

Junnan Li[1] and Nikolay Kornienko[1]*

[1]Department of Chemistry, Université de Montréal, 1375 Avenue Thérèse-Lavoie-Roux, Montréal, QC H2V 0B3, Canada.

*E-mail: nikolay.kornienko@umontreal.ca

**Abstract**:

Electrosynthetic techniques are gaining prominence across the fields of chemistry, engineering and energy science. However, most works within the direction of synthetic heterogeneous electrocatalysis focus on water electrolysis and $CO_2$ reduction. In this work, we moved to expand the scope small molecule electrosynthesis by developing a synthetic scheme which couples $CO_2$ and $NH_3$ at a gas-liquid-solid triple-phase boundary to produce species with C-N bonds. Specifically, by bringing in $CO_2$ from the gas phase and $NH_3$ from the liquid phase together over solid copper catalysts, we have succeeded in forming formamide and acetamide products for the first time. In a subsequent complementary step, we have combined electrochemical analysis and a newly developed *operando* spectroelectrochemical method, capable of probing the aforementioned gas-liquid-solid boundary, to extract an initial level of mechanistic analysis regarding the reaction pathways of these reactions and the current system's limitations. We believe that the development and understanding of this set of reaction pathways will play significant role in expanding the community's understanding of on-surface electrosynthetic reactions as well as push this set of inherently sustainable technologies towards widespread applicability.

**Introduction:**

With the increased focus on attaining global sustainability as a means to mitigate climate change and environmental degradation, the development of green technologies to enable the transition is increasingly important. Within this context, renewable electricity-powered electrosynthetic routes towards generating the fuels and chemicals that drive modern society stand to play a significant role if they manage to displace currently used fossil-fuel dependent methods[1-3]. While the recent decade of academic research has largely focused on water electrolysis[4] and $CO_2$ reduction[5] to generate $H_2$ and carbon-based fuels, respectively, there is no reason that the scope of heterogeneous electrosynthesis needs to be limited to these reactions. In principle, almost any commodity chemical can be synthesized from abundant small molecule building blocks ($N_2$, $H_2O$, $CH_4$, biomass…) if the proper catalytic system would be developed.[6] The difficulty in realizing this ambitious aim is that at this point, only relatively simple electrosynthetic reactions over heterogeneous catalysts are well-understood and can be carried out at high rates and selectivity.

To this end, we moved to develop electrosynthetic routes to C-N bond formation using $CO_2$ and $NH_3$ as model building blocks. In general, despite the biological, societal and technological importance of many chemicals containing C-N bonds[7-10], the area of electrochemical C-N bond formation is very nascent. While biological[11-13] and chemical[7, 14] routes are established, only few examples exist in carrying out C-N coupling on heterogeneous electrocatalysts. Thus, new reaction schemes and mechanistic insights in this context stand to provide a significant boost to the community[15-21]. In the context of heterogeneous catalysis, urea has previously been synthesized from co-electrolysis of $N_2$ or nitrate together with $CO_2$.[16, 18, 19, 21] α-keto acids have been converted into amino acids with hydroxylamine as a N-source.[22] Further, CO was co-electrolyzed with a series of different amines to generate amide products[17]. Finally, a host biomass-derived furans were reductively aminated to produce to amine derivatives.[20] To expand the scope of possibilities of heterogeneously catalyzed C-N bond formation, we have developed a novel electrosynthetic scheme. Here, $NH_3$ from the liquid phase would react with $CO_2$ from the gas phase over a heterogeneous Cu catalyst at a gas-liquid-solid boundary (Fig.1). As such, we generated formamide and acetamide from $CO_2$ and $NH_3$ for the first time, opening up a new avenue to the research community. Through quantitative reaction analysis and newly-developed infrared spectroelectrochemical investigations, we have built up a set of mechanistic insights in terms of elucidating reaction pathways and performance limitations, thus enabling the rational design of next-generation electrosynthetic systems.

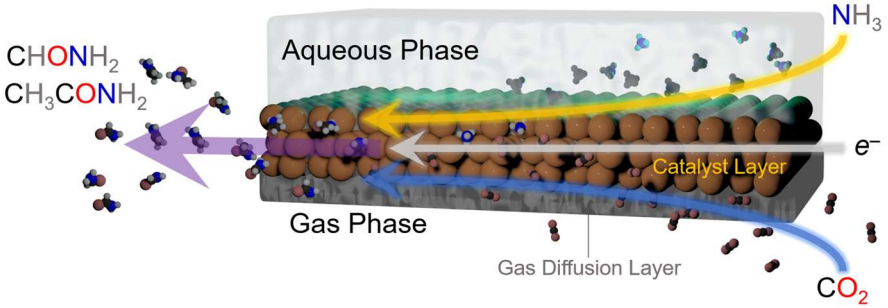


**Figure 1:** Illustration of electrosynthetic strategy for on-surface C-N bond formation. A gas diffusion electrode was employed in which the reactants were simultaneously brought in from the gas phase ($CO_2$) and from the liquid phase ($NH_3$) and reacted over a solid Cu catalyst onto which an electrochemical potential was applied. This configuration enabled the generation of formamide and acetamide C-N bond containing products.

**Catalyst Construction:**

As a starting point, we selected two types of commercially available copper catalysts, Cu and CuO nanoparticles, for use in our study. Copper was selected as the element of choice because it has an intermediate binding energy to many carbon-based species.[23] This is a favorable metric in $CO_2$ reduction because it enables the retention of surface intermediates en route to the formation of highly reduced products like ethylene. At the same time, the binding strength to the intermediates is not too high to poison the surface. Thus, we reasoned that the same argument would apply in retaining $CO_2$ reduction intermediates long enough for their coupling with $NH_3$ would hold. While there is a plethora of studies of Cu-based catalysts and how defects, surface crystallographic facets, ligands, oxygen species and more dictate reaction pathways, we chose to leave such catalyst modifications for future follow-up works given the novelty of this reaction path.[23] The one variable that we did choose to investigate was the use of CuO as a starting material, which when reduced to Cu under cathodic potentials would likely contain additional binding sites in the form of defects. As such, Cu (Fig. 2a) and CuO (Fig. 2b) with no deliberate surface or structural modifications and size around 100 nm were used. The catalysts were mixed with a nafion binder to generate an ink which was then drop cast onto a gas diffusion electrode. This type of electrode featured a gas-permeable gas diffusion layer and microporous layer through which $CO_2$ could reach the catalyst layer on top (Fig. 2c). The goal here was to drive the C-N coupling reaction at the interfacial gas-liquid-solid boundary. This type of electrode geometry is particularly beneficial in overcoming the limited solubility of $CO_2$ in aqueous electrolyte; the use of alkaline electrolytes that minimize the competing hydrogen evolution reaction at industrially relevant current densities (hundreds of $mA/cm^{-2}$).[24, 25] The reaction cell was a modified one from those commonly employed in the field in order to minimize reaction volume and consequently maximize sensitivity for products. In particular, we employed an open cell design in which approximately 1 mL volume of electrolyte was used (Fig. S2).

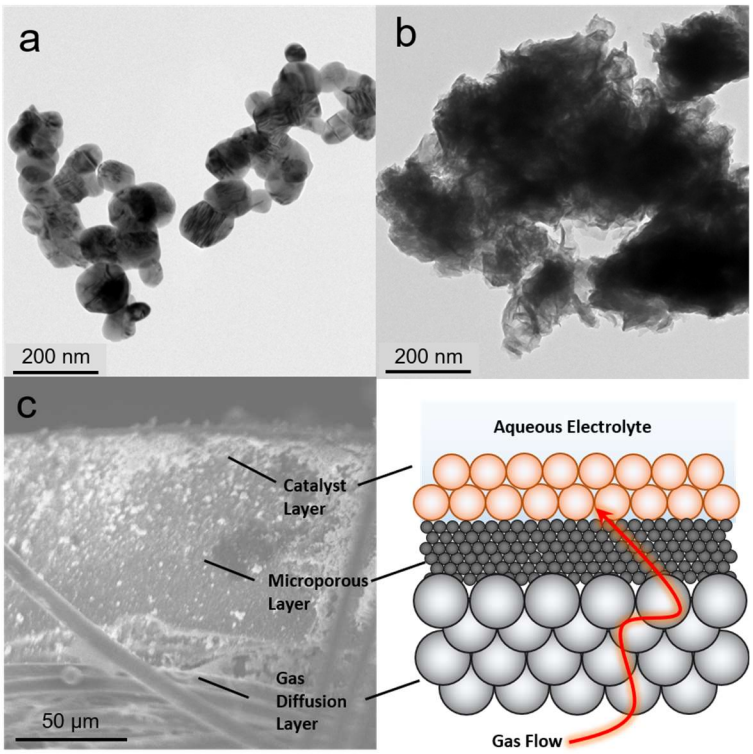

**Figure 2:** The Cu (a) and CuO (b) catalyst particles were first characterized through transmission electron microscopy to probe their size and morphology. They were drop-cast onto a gas-diffusion electrode, which was characterized through scanning electron microscopy (c). The gas diffusion electrode consisted of several layers, illustrated with the graphic as a simplified representation. This electrode enabled gaseous reactants ($CO_2$ in this case) to reach a solid electrocatalyst (Cu/CuO) and circumvent the limited solubility of $CO_2$.

**Electrosynthetic Studies:**

We employed 1M KOH as an electrolyte for this work as highly alkaline electrolytes tend to minimize the hydrogen evolution reaction (HER) and thus favor $CO_2$ reduction. $NH_3$ was set to be a model nitrogen source. In the long term, $NH_3$ would ideally be replaced directly by $N_2$ as an abundant feedstock, though at this stage, electrochemically activating $N_2$ not yet a well-established reaction[26, 27]. Formamide (Fig. 3a) and acetamide (Fig. 3b) primary amines were two likely C-N coupled products that could be formed from $NH_3$ and $C_1$ and $C_2$ surface intermediates via several proton and electron transfer steps. In a gas-diffusion based electrochemical cell, both Cu and CuO featured an onset of catalytic current around 0V vs. the reversible hydrogen electrode (RHE) and reached 100 mA/cm$^2$ by -1.0$V_{RHE}$ (Fig. S3 a,b). The addition of $NH_4OH$ (present as mainly $NH_3$ in alkaline solutions) to the electrolyte did not significantly alter the current density. Product quantification with gas chromatography (GC) and NMR revealed formate and $H_2$ to be the two main products from the reaction (Fig. S4). However, on both Cu and CuO, formamide and acetamide were detected and were formed with partial current densities of ranging from 0.1 to 1.2 mA/cm$^2$, depending on the applied potential (Fig. 3c, d). While the Faradaic efficiency for their formation was rather modest, peaking at approximately 1% (Fig. 3e, f), this study constitutes the first report of their synthesis from $CO_2$ and $NH_3$ building blocks. In addition, performing the same measurements in a standard 3-electrode setup with the working electrode completely immersed in the aqueous phase did not result in any detectible C-N products, even after 24 hrs of electrolysis. This is likely due to a lower $CO_2$ concentration and lack of an alkaline environment that together promote a high degree of strongly bound C-based intermediates needed to couple with $NH_3$. As a control experiment, $CO_2$ electrolysis alone only resulted in formate (Fig. 3g) and acetate (Fig. 3h) products that gave rise to NMR peaks in the range of interest. Interestingly, while the formate selectivity was very high (up to 90%) without $NH_3$, $NH_3$ addition to the electrolyte decreased this value by a factor of 2-3 (Fig. S5) while promoting hydrogen evolution. While this performance is not yet sufficient for economically competitive electrosynthesis, improving the initial system should certainly be feasible as one could point to the rapid maturation of $CO_2$ electrosynthetic technologies over the last decade[2].

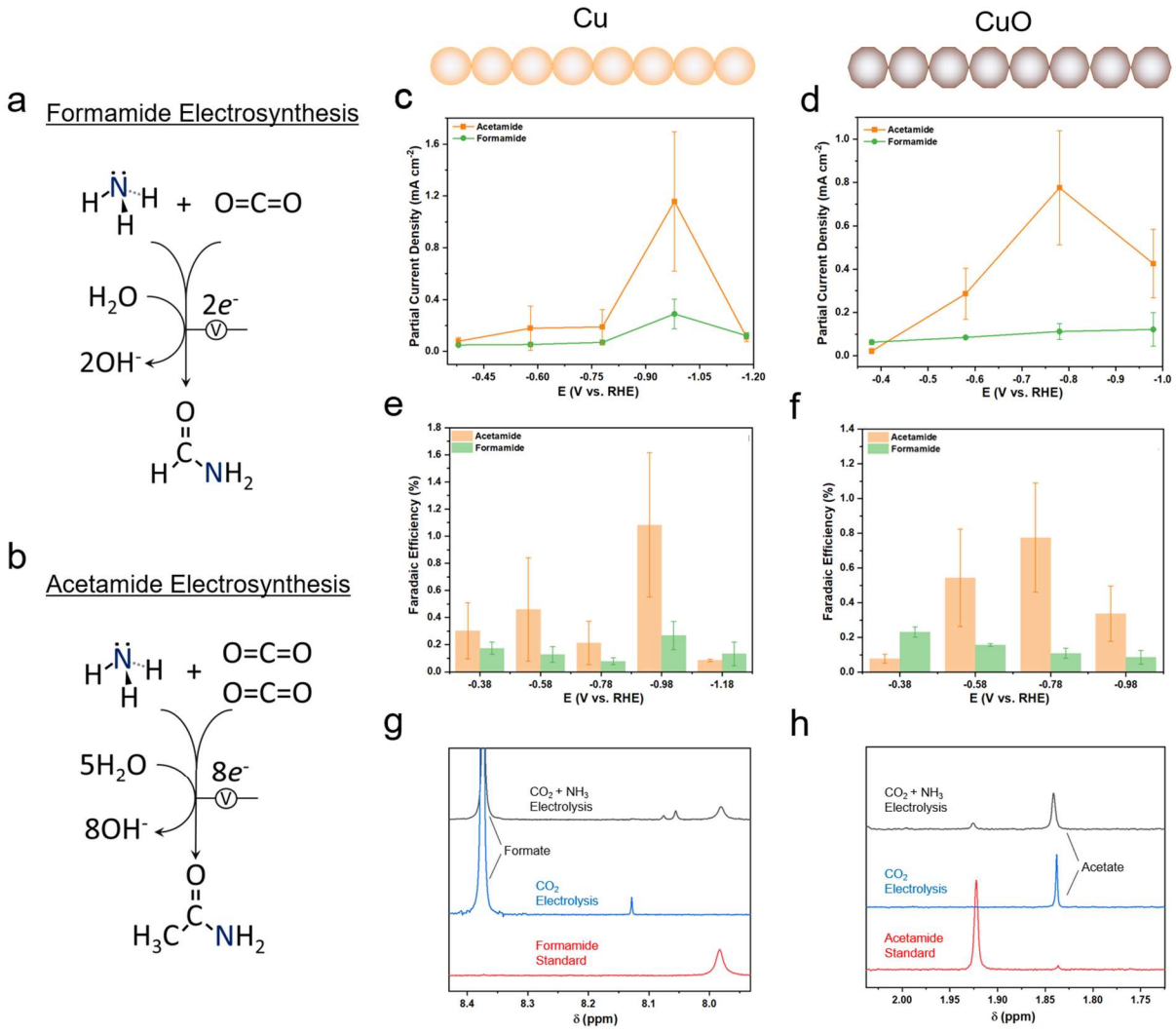


**Figure 3:** The overall reaction is depicted for formamide involves 2 electrons and 1 $CO_2$ molecule (a) while acetamide electrosynthesis entails 8 electrons and 2 $CO_2$ molecules (b). In the gas diffusion electrode cell with a 1M KOH electrolyte, 6SCCM $CO_2$ flow, and the optimized (5M or 1M) concentration of $NH_3$, formamide (c) and acetamide (d) were quantified and their partial current densities derived from the resulting concentrations. The Faradaic efficiencies for both products were similarly obtained for Cu (a) and CuO (b) catalysts. Representative NMR spectra are shown for formamide (g) and acetamide (h) from which the concentrations are quantified.

## Infrared Spectroscopy

To extract a further level of insights into the formamide and acetamide electrosynthetic pathways, we turned to infrared spectroscopy. This technique measures the vibrational modes of species within the electrolyte and on the catalyst surface. Typically, measurements are carried out in difference mode, using the system at open circuit as a refence and subtracting this from the spectra under applied bias, thus detecting the appearance of new species (positive bands) and disappearance of others (negative bands). The spectroscopic measurements were carried out in an attenuated-total reflection (ATR) mode using a home-built spectroelectrochemical setup (Fig. 4a). Briefly, a thin layer of aqueous electrolyte (KOH or

KOH + $NH_3$) was on top of the diamond-coated ZnSe ATR crystal. The Cu catalyst layer/microporous layer/gas diffusion layer composite electrode was placed overtop so that the gas/liquid/solid boundary could be spectroscopically probed. In this configuration, the liquid was in static mode while the gas flowed above. The ability to probe this region was evident when measuring the difference spectrum between Ar flow and $CO_2$ flow in this configuration, which shows the presence of both gaseous and dissolved $CO_2$ and carbonate species (Fig. S12)[28].

Under an argon flow with $NH_3$ and no $CO_2$, the main spectral features corresponded mainly to that of water and to that of $NH_3$ (Fig. S13-15).[28] Under the same conditions but with $CO_2$ flowing in place of Ar, a new set of positive bands appeared which can primarily be assigned to carbonate and bicarbonate species coming from $CO_2$ reacting with the KOH electrolyte and changes in pH (Fig. S14)[29]. Such species been shown to spontaneously appear at the gas-liquid-solid interface in similar conditions with Raman measurements.[30] While spectral features in the 1800-2100 $cm^{-1}$ are noted where the C-O stretch of *CO is located, the inherent absorbance of our diamond-coated ATR crystal makes this region rather noisy rendering bands here more difficult to fit and explicitly assign.

In the presence of both $CO_2$ and $NH_3$, new bands appeared at both the region containing N-H bonds from the generation of $NH_4^+$ (Fig. 4b).[31] As a method of validation, spectra were also acquired with $^{15}NH_3$ instead of $^{14}NH_3$ (Fig. S13). Indeed, the isotope effect was noted via a red-shift around 30 $cm^{-1}$ for bands at both spectral regions. Interestingly, the intensity of the bicarbonate band at 1300 $cm^{-1}$ saturated very early with only $CO_2$ present, but continually gained intensity under increasingly higher currents when $NH_3$ was present (Fig. S13). A possible explanation for this could that be the presence of $NH_3$ diminishes the concentration of $CO_2$/carbonate reactants near the interface at low currents.

Finally, as (bi)carbonate species dominate the IR spectra, we opted to subtract spectra of the catalyst systems operating at -1 mA from those at -200 mA, as the (bi)carbonate species are mostly saturated and those with smaller spectral contributions could be visualized (Fig. 4c). Indeed, for the CuO catalyst in the presence of $CO_2$ and $NH_3$, the evolution of positive spectral features (1645, 1598, 1547 1402 and 1096 $cm^{-1}$) and negative bands (1660, 1425 and 1362 $cm^{-1}$) were noted. While a fully unambiguous assignment at this stage is not yet possible, we note that these spectral features correlate well with those previously assigned to $*COO^-$ and *COOH and these species are thus our tentative assignments.[32-34] The complete set of plausible band assignments is compiled in table 1.

As formate is the dominant product in each of these systems, it would seem reasonable to have a substantial $*COO^-$ surface coverage and thus this is our tentative assignment. While the precise mechanism of formate electrosynthesis is still under debate, on copper surfaces, it has been argued through a combination of surface-enhanced Raman spectroscopy and DFT modelling that the all $CO_2$ reduction pathways share a common first intermediate in a $\mu_2$, -C, -O bound $CO_2{}^{*-}$ that subsequently gets hydrogenated en route to formate or protonated to *COOH en route to CO and other $C_2$ downstream products.[35] Thus, the observation of $*COO^-$ and *COOH intermediates being the main ones on the surface would support our product distribution.

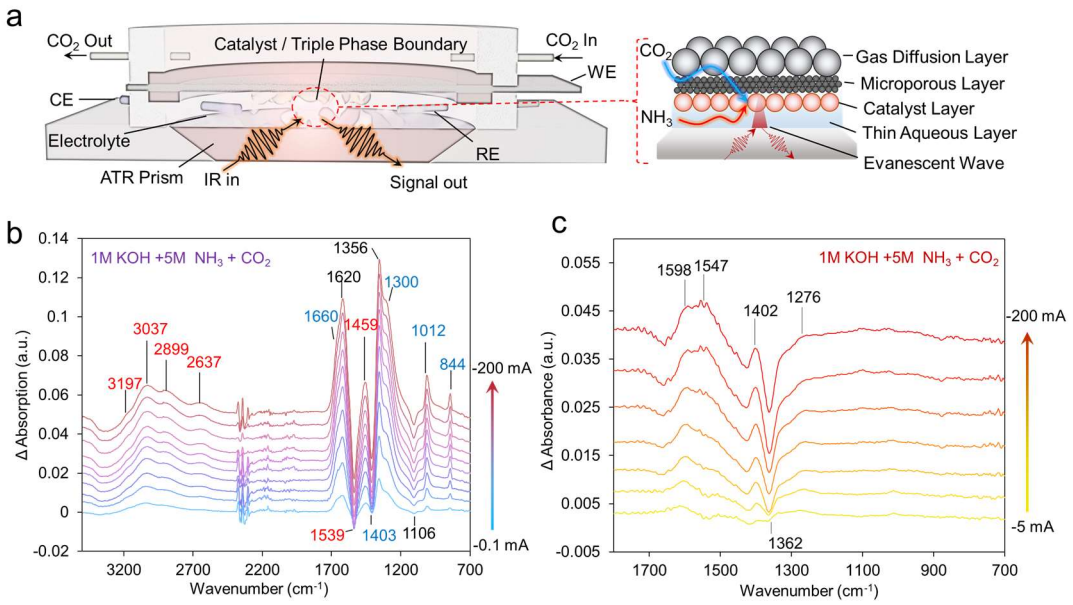


**Figure 4:** Spectroelectrochemical setup enabling *operando* infrared spectroscopic probing of the electrosynthetic reactions in a gas-diffusion electrode cell (a). This setup used a thin electrolyte window with the GDE just overtop to probe both liquid, gas and solid phases. The gas was flowing through while the liquid was static. Using the spectrum at open circuit as the background, spectra under select operating current densities were recorded (b). Subtracting out the bi(carbonate) contributions using the spectra at 1 mA/cm$^2$ as a background, enables the identification of additional species present on the CuO surface (c).

| Band position ($cm^{-1}$) | Species | Figure | Possible Assignment |
|---|---|---|---|
| 1660 | $HCO_3^-$ | 4b | $\nu_{as}$(–C–O)[28] |
| 1356 | $HCO_3^-$ | 4b | $\nu$(–C–O)[28] |
| 1300 | $HCO_3^-$ | 4b | $\delta$(C–OH)[28] |
| 1012 | $HCO_3^-$ | 4b | $\nu_{as}$(C–OH)[28] |
| 844 | $HCO_3^-$ | 4b | $\nu_s$(C-OH)[36] |
| 1459 | $CO_3^{2-}$ | 4b | $\delta$(–NH)[28] |
| 3197 | $NH_4^+$ | 4b | $\nu$(N-H)[31] |
| 3037 | $NH_4^+$ | 4b | $\nu$(N-H)[31] |
| 2899 | $NH_4^+$ | 4b | $\nu$(N-H)[31] |
| 1459 | $NH_4^+$ | 4b | $\nu$(N-H)[31] |
| 1645 | $H_2O$ | 4c | $\delta$(H-O-H) |
| 1598 | *$COO^-$ | 4c | $\nu_{as}(COO^-)$[35] |
| 1547 | *$COO^-$ | 4c | $\nu_{as}(COO^-)$[33] |
| 1402 | *$COO^-$ | 4c | $\nu_s(COO^-)$[33, 34] |
| 1276 | *COOH | 4c | $\nu$COOH, OH-deformation[33] |

**Table 1:** Peaks detected and plausible assignments from infrared experiments.

While this study used $NH_3$ as a starting point for generating C-N bonded products, ideally, the nitrogen source would be gaseous $N_2$ as the technology matures and scales. To this end, we have explored as an intermediate progression the co-reduction of nitrate and nitrite ions in place of $NH_3$ to generate the same products. The experimental procedure was the same except that the nitrate/nitrite was in place of $NH_3$ in the electrolyte, with optimized concentrations of $NO_2/NO_3$ (Fig. S15, 16). Over a Cu catalyst at -0.98V vs. RHE, formamide and acetamide were indeed formed, albeit at reduced faradaic efficiencies and partial current densities (Fig. 5). While a comprehensive set of electroanalytical and spectroscopic experiments is outside of the scope of this initial work, the results indicate that there is much to discover in optimizing the reduction pathways of both C and N sources en route to C-N bond formation. A likely reaction pathway that would explain our results would be the reduction of nitrate/nitrite on the electrode surface to $NH_3$, which then couples with intermediates from $CO_2$ reduction. We believe that the $NH_3$ on the other hand is not directly bound to the surface but rather located in the near-surface region (Fig. S18). Its presence seems to hinder both hydrogen evolution and $CO_2$ reduction, likely through inhibiting reactant diffusion to active sites on the catalyst. The tendency to enhance hydrogen evolution likely stems through an enhanced hinderance of $CO_2$ diffusion as opposed to that of water molecules.

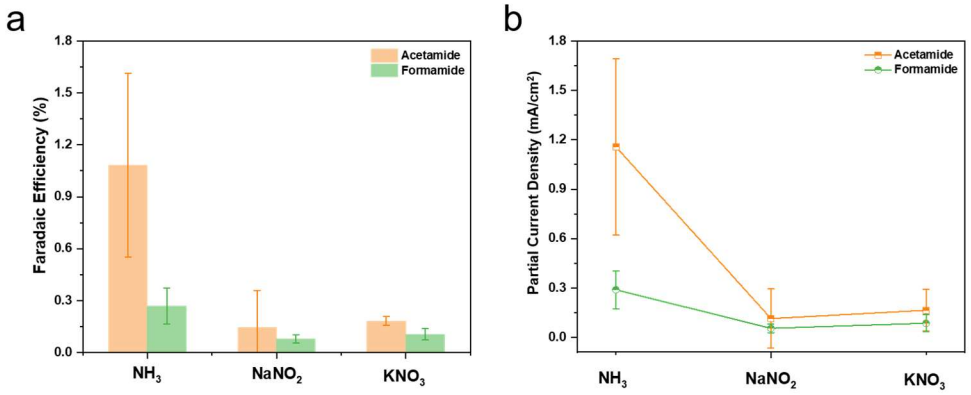


**Figure 5:** In the equivalent reaction setup as in figure 3 with Cu catalysts and $NO_2^-$ (0.5M) or $NO_3^-$(1M) in place of $NH_3$ at -0.98V vs. RHE, formamide and acetamide were generated. The Faradaic efficiencies (a) and partial current densities (b) for their generation were compared to those from using $NH_3$.

Finally, we moved to optimize the C-N product generation of our system. We first screened the parameters of KOH concentration, Cu catalyst loading, and cation identity (Fig. S21). The biggest enhancement in acetamide generation came from a higher Cu loading (10 mg/cm$^2$ vs. 2 mg/cm$^2$). We attribute this to the propensity of the catalyst layer to generate a higher amount of highly reduced $C_2$ intermediates through the thicker Cu film. Further, a lower KOH concentration and a change from $K^+$ to $Cs^+$ also yielded selectivity enhancements for acetamide, possible due to a more favorable near-surface reaction environment to stabilize reaction intermediates en route to the $C_2$ species that can couple with $NH_3$ to generate formamide. Interestingly, the activity enhancements were not realized for formamide. This can be rationalized as the factors necessary for favorizing a $CO_2$ reduction pathway to $C_2$ species as not being necessary for formamide, which is more dependent on the initial *$COO^-$ intermediate coupling with $NH_3$.

Then, with all three optimized parameters incorporated (0.1M CsOH electrolyte, 10 mg/cm$^1$ Cu loading), we compared the Faradaic efficiency and partial current densities for the optimized system to that of the original from Fig. 2 across the experimental potential range (Fig. 6).

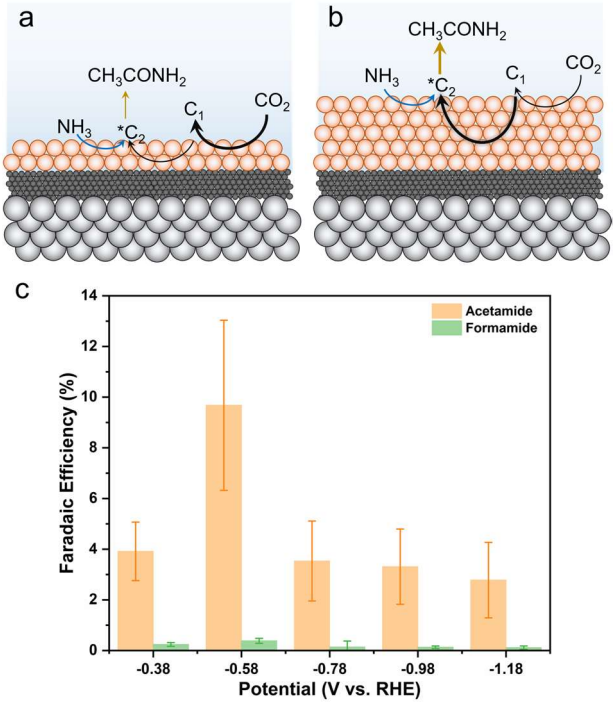


**Figure 6:** A thicker catalyst loading was found to promote acetamide formation. Thin layers tend to form $C_1$ products at a greater rate (a) while increasing the layer thickness leads to further reduction and accumulation of $C_2$ intermediates that can be used for C-N bond formation (b). As such, an optimized Cu loading of 10 mg/cm$^2$ resulted in up to 10% acetamide selectivity (c).

We believe that the formate and formamide electrosynthetic pathways are linked on the Cu surface in that they share a common intermediate. This belief is backed by their similarity in chemical structure. Considering that the formation of C-N containing products involves the nucleophilic attack of a carbon atom by the lone pair on the nitrogen atom of ammonia, an activated, yet exposed carbon species that could couple with ammonia for formamide generation could be that of the $\mu_2$, -C, -O bound *$CO_2^-$[35]. There would then be a competition between hydrogenation of this species to produce formate or a nucleophilic attack to eventually form formamide (Fig. 7a). This branching point is also supported by the fact that using 1M formate instead of $CO_2$ as the C-source in otherwise identical conditions did not lead to any detectable formamide and only a small amount of acetamide (Figure S14).

On the other hand, acetamide synthesis likely shares a reaction pathway with acetate and thus requires a $C_2$ intermediate to already be present[17]. The branching for this step also plausible occurs at the *$CO_2^-$ intermediate, which is converted to *CO. The coupling of 2 *CO molecules is thought to be a key step to generating $C_2$ products (acetate, ethanol, ethylene). The *CCO intermediate was recently proposed as a likely candidate for this through a DFT analysis of acetamide synthesis via CO and $NH_3$ building blocks and would be a plausible candidate for our work as well.[17] The middle carbon would thus be subject to nucleophilic attack by the $NH_3$ in this pathway where it diverges from the acetate pathway as

previously postulated.[17] The enhancement of $C_2$ intermediates such as this with a thick catalyst layer is postulated to be the main driving factor for its generation.

The two pathways presented here are not so different than what occurs in enzymatic catalytic pockets, where an electron rich amine couples with an electron poor carbon[11-13] and one can imagine that generating on-surface catalytic pockets in a synthetic system to promote this reaction would lead to further enhancements of electrosynthetic selectivity. As the nucleophilic attach is by the ammonia nitrogen is a thermodynamically downhill step, reduction potential for both of these reactions is still dictated by that necessary to reduce $CO_2$.

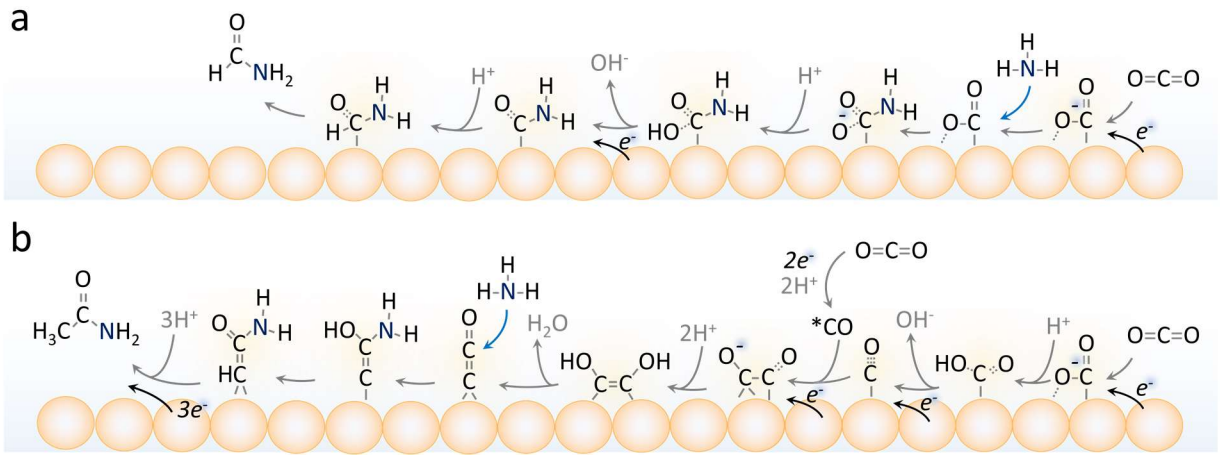


**Figure 7:** Plausible surface reaction pathways in the electrosynthetic process of formamide (a) and acetamide (b) generation. Formamide generation depends on $NH_3$ coupling with the first reaction intermediate while acetamide generation requires highly reduced $C_2$ intermediates to be present on the catalyst surface. For simplicity, the donation of a proton to surface intermediates via $H_2O \rightarrow OH^-$ is depicted as $\rightarrow H^+$.

**Concluding Remarks:**

While two new reaction pathways have been discovered in formamide and acetamide electrosynthesis using $CO_2$ and $NH_3$ building blocks, many avenues are now opened for further understanding and improving the efficiency of these reactions. First, while we used commercially purchased Cu and CuO nanoparticles as a readily available model system, they feature a diversity of active sites, defects, (sub)surface oxygen species, and exposed crystallographic facets. It is entirely possible that each of these factors may influence the reaction like they do in the electrosynthesis of carbon-based products via $CO_2$ reduction. A rational way forward would be the precise study of well-defined copper catalysts in which the nature surface-active sites are known and with complementary theoretical modelling of likely reaction pathways on these surfaces. Further, it is not known if Cu is the only catalyst capable of carrying out this reaction and if formate-selective metals like Sn and Bi would thus be more effective at formamide synthesis. In addition, we have developed an *operando* infrared spectroscopic method for the first time that was used to help understand this reaction pathway but

additional complementary techniques such as Raman and X-ray absorption would contribute immensely valuable pieces to this puzzle.[37]

This principal significance to this work is the electrosynthetic reaction discovery which we envision will accelerate the adoption of electrosynthetic methodology at large in both the academic and industrial domains. While $NH_3$ is used as the model nitrogen source and nitrate and nitrite as further examples, eventually, this may be replaced by $N_2$ in a fully sustainable nitrogen cycle. In general, the capacity to drive heteroatomic surface coupling reactions with renewable-electricity powered systems stands to open up an abundance of decentralized green synthetic routes in place of heavy-infrastructure requiring fossil fuel based thermochemical approaches. In parallel, there is much more fundamental chemistry to be discovered through the use of new interfaces, spectroscopic methodology, and catalytic systems.

**Acknowledgements:**

N.K. and J.L acknowledge NSERC Discovery Grant RGPIN-2019-05927

**Author Contributions:**

N.K and J.L both designed the project, carried out experiments, processed data, contributed intellectual insights and wrote the manuscript.

**Competing Interests:**

None to declare

**References:**

1. J. Masa, C. Andronescu and W. Schuhmann, *Angew. Chem. Int. Ed.*, 2020, **59**, 15298-15312.
2. P. De Luna, C. Hahn, D. Higgins, S. A. Jaffer, T. F. Jaramillo and E. H. Sargent, *Science*, 2019, **364**, eaav3506.
3. M. Wang, M. A. Khan, I. Mohsin, J. Wicks, A. H. Ip, K. Z. Sumon, C.-T. Dinh, E. H. Sargent, I. D. Gates and M. G. Kibria, *Energy Environ. Sci.*, 2021, DOI: 10.1039/D0EE03808C.
4. J. Kibsgaard and I. Chorkendorff, *Nat. Energy*, 2019, **4**, 430-433.
5. M. B. Ross, P. De Luna, Y. Li, C.-T. Dinh, D. Kim, P. Yang and E. H. Sargent, *Nat. Catal.*, 2019, **2**, 648-658.
6. Z. J. Schiffer and K. Manthiram, *Joule*, 2017, **1**, 10-14.
7. O. I. Afanasyev, E. Kuchuk, D. L. Usanov and D. Chusov, *Chemical Reviews*, 2019, **119**, 11857-11911.
8. J. R. Dunetz, J. Magano and G. A. Weisenburger, *Org. Process Res. Dev.*, 2016, **20**, 140-177.
9. X. Guo, A. Facchetti and T. J. Marks, *Chemical Reviews*, 2014, **114**, 8943-9021.
10. M. Höhne and U. T. Bornscheuer, *ChemCatChem*, 2009, **1**, 42-51.
11. M. D. Patil, G. Grogan, A. Bommarius and H. Yun, *ACS Catal.*, 2018, **8**, 10985-11015.
12. O. Mayol, K. Bastard, L. Beloti, A. Frese, J. P. Turkenburg, J.-L. Petit, A. Mariage, A. Debard, V. Pellouin, A. Perret, V. de Berardinis, A. Zaparucha, G. Grogan and C. Vergne-Vaxelaire, *Nat. Catal.*, 2019, **2**, 324-333.
13. G. A. Aleku, S. P. France, H. Man, J. Mangas-Sanchez, S. L. Montgomery, M. Sharma, F. Leipold, S. Hussain, G. Grogan and N. J. Turner, *Nat. Chem.*, 2017, **9**, 961-969.
14. H. Kim and S. Chang, *ACS Catal.*, 2016, **6**, 2341-2351.
15. J. E. Kim, S. Choi, M. Balamurugan, J. H. Jang and K. T. Nam, *Trends Chem.*, 2020, **2**, 1004-1019.

16. C. Chen, X. Zhu, X. Wen, Y. Zhou, L. Zhou, H. Li, L. Tao, Q. Li, S. Du, T. Liu, D. Yan, C. Xie, Y. Zou, Y. Wang, R. Chen, J. Huo, Y. Li, J. Cheng, H. Su, X. Zhao, W. Cheng, Q. Liu, H. Lin, J. Luo, J. Chen, M. Dong, K. Cheng, C. Li and S. Wang, *Nat. Chem.*, 2020, **12**, 717-724.
17. M. Jouny, J.-J. Lv, T. Cheng, B. H. Ko, J.-J. Zhu, W. A. Goddard and F. Jiao, *Nat. Chem.*, 2019, **11**, 846-851.
18. N. Meng, Y. Huang, Y. Liu, Y. Yu and B. Zhang, *Cell Rep. Phys. Sci.*, 2021, **2**, 100378.
19. Y. Feng, H. Yang, Y. Zhang, X. Huang, L. Li, T. Cheng and Q. Shao, *Nano Lett.*, 2020, **20**, 8282-8289.
20. J. J. Roylance and K.-S. Choi, *Green Chem.*, 2016, **18**, 5412-5417.
21. M. Shibata, K. Yoshida and N. Furuya, *J. Electrochem. Soc.*, 1998, **145**, 2348-2353.
22. T. Fukushima and M. Yamauchi, *Chem. Commun.*, 2019, **55**, 14721-14724.
23. S. Nitopi, E. Bertheussen, S. B. Scott, X. Liu, A. K. Engstfeld, S. Horch, B. Seger, I. E. L. Stephens, K. Chan, C. Hahn, J. K. Nørskov, T. F. Jaramillo and I. Chorkendorff, *Chemical Reviews*, 2019, **119**, 7610-7672.
24. D. Higgins, C. Hahn, C. Xiang, T. F. Jaramillo and A. Z. Weber, *ACS Energy Lett.*, 2019, **4**, 317-324.
25. F. P. García de Arquer, C.-T. Dinh, A. Ozden, J. Wicks, C. McCallum, A. R. Kirmani, D.-H. Nam, C. Gabardo, A. Seifitokaldani, X. Wang, Y. C. Li, F. Li, J. Edwards, L. J. Richter, S. J. Thorpe, D. Sinton and E. H. Sargent, *Science*, 2020, **367**, 661-666.
26. S. L. Foster, S. I. P. Bakovic, R. D. Duda, S. Maheshwari, R. D. Milton, S. D. Minteer, M. J. Janik, J. N. Renner and L. F. Greenlee, *Nat. Catal.*, 2018, **1**, 490-500.
27. D. Liu, M. Chen, X. Du, H. Ai, K. H. Lo, S. Wang, S. Chen, G. Xing, X. Wang and H. Pan, *Adv. Func. Mater.*, 2021, **31**, 2008983.
28. F. Milella and M. Mazzotti, *React. Chem. Eng.*, 2019, **4**, 1284-1302.
29. R. Kas, O. Ayemoba, N. J. Firet, J. Middelkoop, W. A. Smith and A. Cuesta, *ChemPhysChem*, 2019, **20**, 2904-2925.
30. X. Lu, C. Zhu, Z. Wu, J. Xuan, J. S. Francisco and H. Wang, *J. Am. Chem. Sci.*, 2020, **142**, 15438-15444.
31. P. P. Sethna, H. D. Downing, L. W. Pinkley and D. Williams, *J. Opt. Soc. Am.*, 1978, **68**, 429-431.
32. M. F. Baruch, J. E. Pander, J. L. White and A. B. Bocarsly, *ACS Catal.*, 2015, **5**, 3148-3156.
33. N. J. Firet and W. A. Smith, *ACS Catal.*, 2017, **7**, 606-612.
34. S. Zhu, B. Jiang, W.-B. Cai and M. Shao, *J. Am. Chem. Sci.*, 2017, **139**, 15664-15667.
35. I. V. Chernyshova, P. Somasundaran and S. Ponnurangam, *Proc. Natl. Acad. Sci. U.S.A.*, 2018, **115**, E9261.
36. E. Garand, T. Wende, D. J. Goebbert, R. Bergmann, G. Meijer, D. M. Neumark and K. R. Asmis, *J. Am. Chem. Sci.*, 2010, **132**, 849-856.
37. Y. Zhu, J. Wang, H. Chu, Y.-C. Chu and H. M. Chen, *ACS Energy Lett.*, 2020, **5**, 1281-1291.

Supplementary information for:

# Electrochemically Driven C-N Bond Formation from $CO_2$ and Ammonia at the Triple-Phase Boundary

Junnan Li[a] and Nikolay Kornienko[a]*

[a]*Department of Chemistry, Université de Montréal, 1375 Ave. Thérèse-Lavoie-Roux, Montréal, QC H2V 0B3*

*email: Nikolay.kornienko@umontreal.ca

**Characterization:**

Scanning electron microscopic (SEM) images and EDS were measured using a JEOL JSM-7600F Field Emission SEM microscope. Transmission electron microscopic (TEM) images were performed on JEOL JEM-2100F FEG-TEM, operated at 200 kV.

Electrochemistry and product quantification:

Linearly sweep voltammetry (LSV) was accomplished using a Bio-Logic SP-200 Potentiostat (BioLogic Science Instruments, France). A three-electrode system has been employed by applying the carbon cloth gas diffusion layer (GDL-CT (W1S1009, Fuel Cells Etc.) as the working electrode, Ag/AgCl as the reference electrode and a glassy carbon rod as the counter electrode. While a Hg/HgOH reference is preferred for alkaline conditions due to its higher stability, we needed a small Ag/AgCl electrode to fit within our cell and referenced it periodically to a master Ag/AgCl electrode to ensure that there was no significant potential drift.

The preparation of working electrode followed steps: 10 mg Cu (Alfa Aesar, Copper Nanopowder, 99.9% APS 20-50 nm, Lot P11F044) or CuO (Alfa Aesar, Copper(II) Oxide, nanopowder, Lot Y19E022) commercial catalyst powder (20-50 nm particle size) was added into a mixture with 100 μL $H_2O$, 300 μL ethanol, 25 μL Nafion (5% wt.). After ultrasonic mixing for 10 minutes, 100 μL of the catalyst ink was dropped onto the carbon cloth and allowed to dry naturally under ambient conditions. This led to a Cu loading of approximately 2 mg/cm$^2$. 1M KOH solution with different amounts of $NH_4OH$ was used as the electrolyte in all of the measurements. The LSVs were measured in the range of 0.7 ~ -0.98 V (vs. RHE) at a sweep rate of 20 mV s$^{-1}$. Potentiostatic electrolysis was conducted in a gas diffusion electrode (GDE) cell. Before each electrolysis experiment, 1 mL electrolyte was added into the cell, the flow rate of $CO_2$ is 6mL/min. All reactions were carried out at room temperature (23 ± 1 °C). Bulk electrolysis was carried out with

1M $NH_3$ for Cu and 5M $NH_3$ for CuO as these were the experimentally optimized conditions for C-N product generation rates. Because of the high gas generation rates and bubbling, we opted to carry out measurements in static mode (no flow) and in a 1-compartment cell. While this likely led to some crossover, product re-oxidation at the counter electrode, and an underestimation of the reaction efficiency, this geometry was nonetheless more optimal to minimize electrolyte volume and overcome the bubbling issue.

$NH_3$ was only fed through the liquid phase (as $NH_4OH$) while $CO_2$ was only added in through the gas phase. Further, no products were detected in the gas phase via GC analysis beyond CO, $CH_4$ and $H_2$.

In order to quantify the products of the reaction, gas chromatography (GC, SRI 8610C) and NMR (Bruker AVANCE II 400 se) were performed to reveal the content and composition of the gas and liquid products respectively. A sealed GDE cell was used and connected with the GC. The $CO_2$ flow rate employed was 6 mL/min and the products were probed in flow mode as the outlet from the GDE cell flowed directly through the GC. For NMR analysis, 400 μL liquid electrolyte after an electrolysis run was mixed with 400 μL $D_2O$ to quantify liquid products. For NMR measurements, products were quantified using DMSO as an internal standard and calibration curves for several main products in the liquid phase like formate, acetate and ethanol (Fig. S1). Gaseous products were similarly quantified through the integration of peak area corresponding to various products, which were first measured with a series of calibration curves ($H_2$, CO, $CH_4$, $C_2H_6$…). The GC measurements were also collected in flow mode at 6 SCCM $CO_2$ flow with $N_2$ as the carrier gas in the GC. There was no evidence of nitrogenated products in the gas phase from GC measurements.

Typically, liquid products were acquired after 30 minutes of electrolysis. The Faradaic efficiency (FE) was calculated by using the following formula:

$$\varepsilon_{FE} = \frac{\alpha n F}{Q}$$

where α is electron transfer numbers, n is the moles of the products, F is the Faraday constant (96485 C $mol^{-1}$), Q is the charge passed in total during the reaction.

In-situ infrared (IR) spectroscopy:

IR spectra were acquired on a ThermoFischer Nicolet 380 FTIR-ATR with a ZnSe ATR crystal that was coated with a diamond surface. Typically, 200 scans were acquired for each measurement. A three-electrode GDE cell was used for the in-situ IR experiment. Cu wire was used as counter electrode, Ag/AgCl was used as reference, the above carbon cloth with CuO or Cu as working electrode. The electrolyte employed was 1M KOH with or without $NH_4OH$ under a constant $CO_2$ gas flow. The catalyst, deposited onto a carbon cloth gas diffusion layer (coated with a microporous layer) was facing downwards towards the ATR crystal, with a thin electrolyte layer between. The working electrode was gently pressed with a porous foam stud so that there was still ample gas permeation into the triple-phase boundary that was being probed with the IR evanescent wave.

Raman Spectroscopy: Raman Spectra were collected using a Renishaw Invia system with a 785 nm laser having a 5mW output power. The laser line focus illumination technique was used that spread the laser intensity out over a line and minimized the power concentrated at any one spot. The spectra were collected at full intensity power and a typical collection time was 60 seconds. A water immersion objective (numerical aperture of 0.7, working distance of 1mm) was used to maximize signal intensity. Raman measurements were performed in a standard 3-electrode configuration instead of adapting to a gas-diffusion electrode as an initial test. For *operando* Raman measurements, Ag/AgCl reference and carbon cloth were used as reference and counter electrodes. $N_2$ or $CO_2$ purged 1M KOH or 1M KOH + $NH_4OH$ were used as the electrolyte solutions. The working electrode consisted of Cu NPs loaded onto a Toray carbon paper electrode at approximately the same degree of catalyst loading as for the GDE.

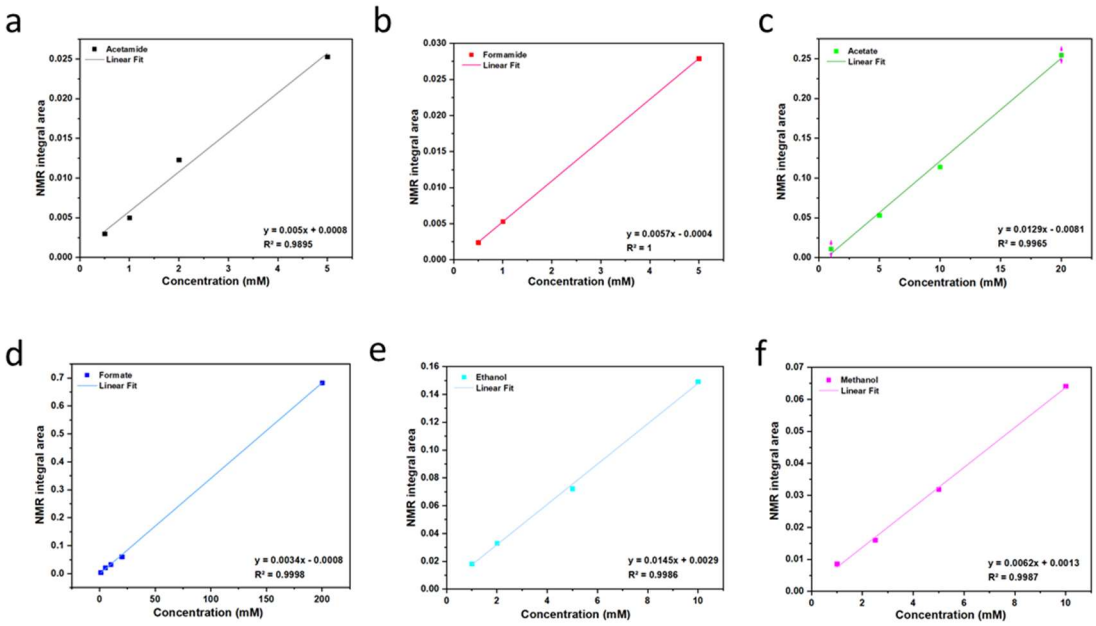


**Figure S1:** NMR calibration curve of (a) Acetamide; (b) Formamide; (c) Acetate; (d) Formate; (e) Ethanol; (f) Methanol. The relative peak area is plotted vs. that of the DMSO internal standard.

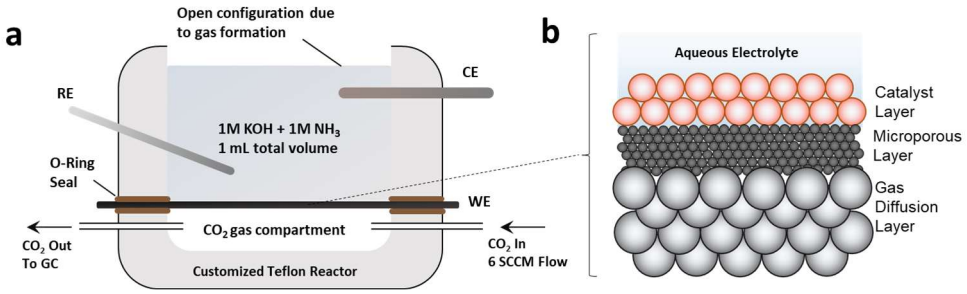


**Figure S2:** Simplified schematic of $CO_2$ reduction reaction cell that enabled high-sensitivity detection of liquid products through the use of minimal (1mL) total electrolyte volume (a) sitting overtop of a gas-diffusion electrode (b). An open configuration was employed as gas bubbles generated throughout the reaction process prohibited using a conventional configuration.

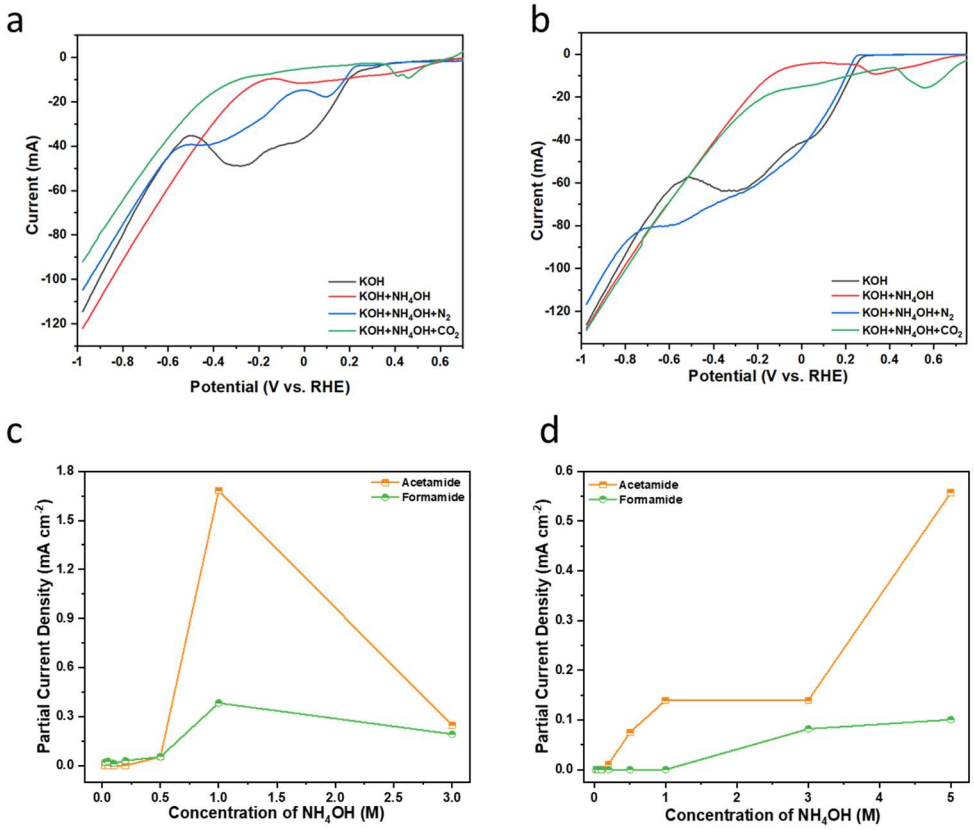


**Figure S3.** LSV curves under different gas environment of (a) Cu; (b) CuO catalyst in different electrolytes. Partial current densities for C-N products from an initial screening of selecting optimal $NH_4OH$ concentrations to add to the electrolyte were also different for Cu (c) and CuO (d).

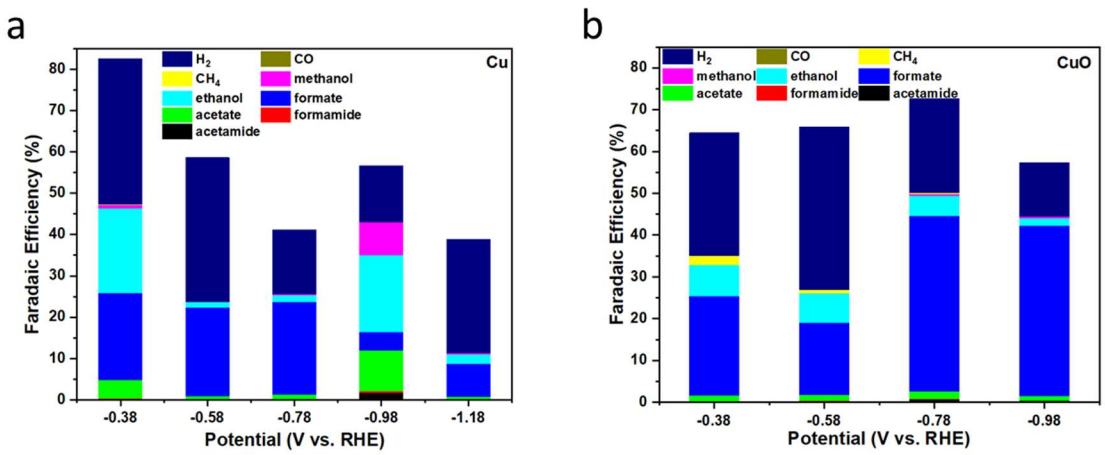


**Figure S4:** Total product quantification for Cu (a) and CuO (b) catalysts.

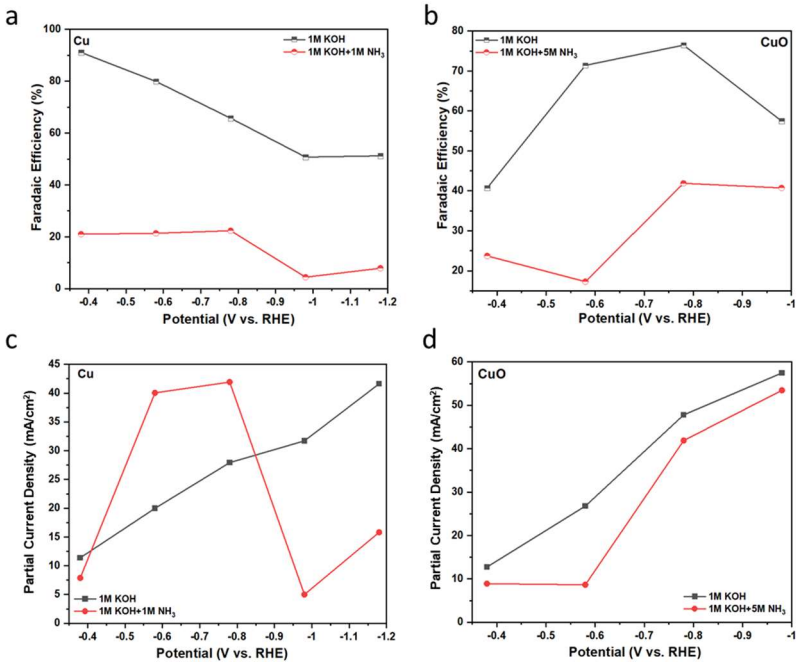


**Figure S5:** Faradaic efficiency and partial current density for formate production in the absence and presence of $NH_3$ for Cu (a, c) and CuO (b, d) catalysts.

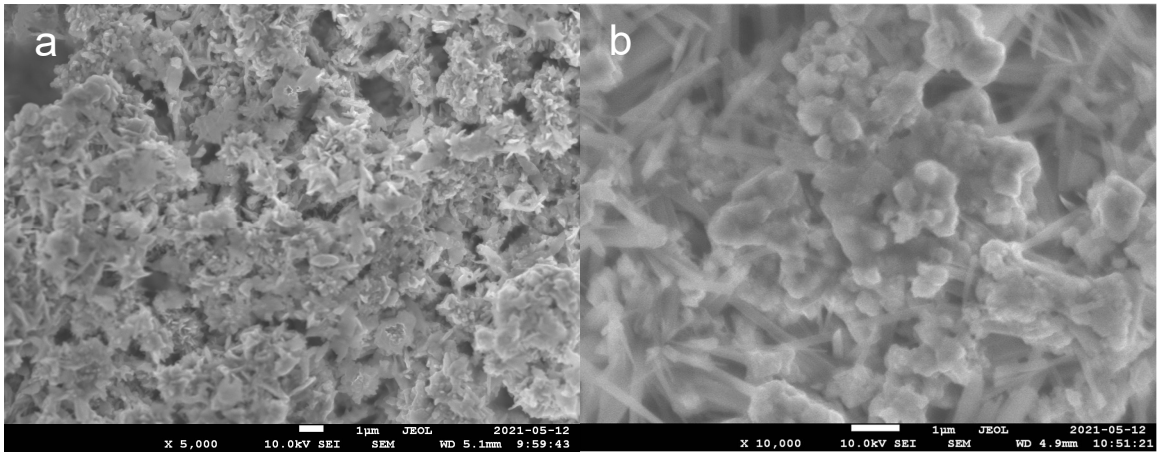


**Figure S6**: SEM images of (a) CuO and (b) Cu after a typical controlled potential electrolysis reaction.

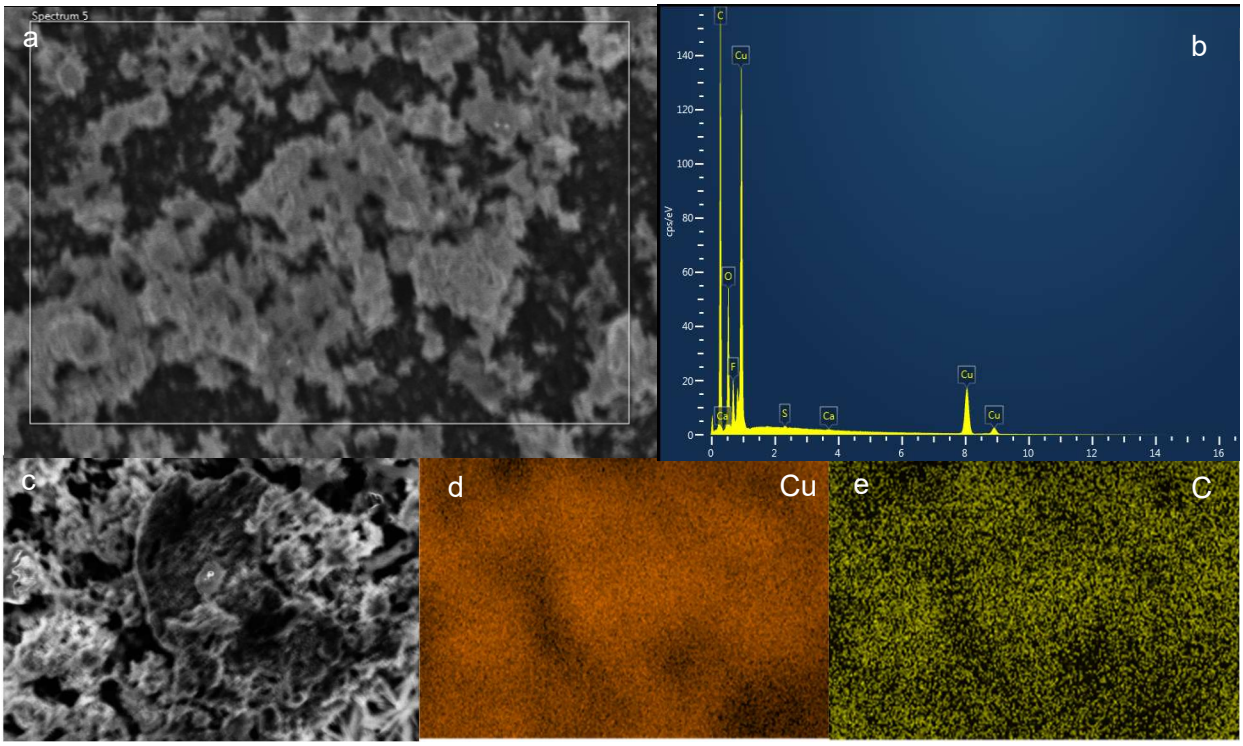


**Figure S7.** (a, c) SEM images of the EDS area; EDS of CuO/C catalyst before reaction (b) EDS spectra; (d) Cu and (e) C element mapping after the reaction (30 min at -0.98V vs. RHE)**.**

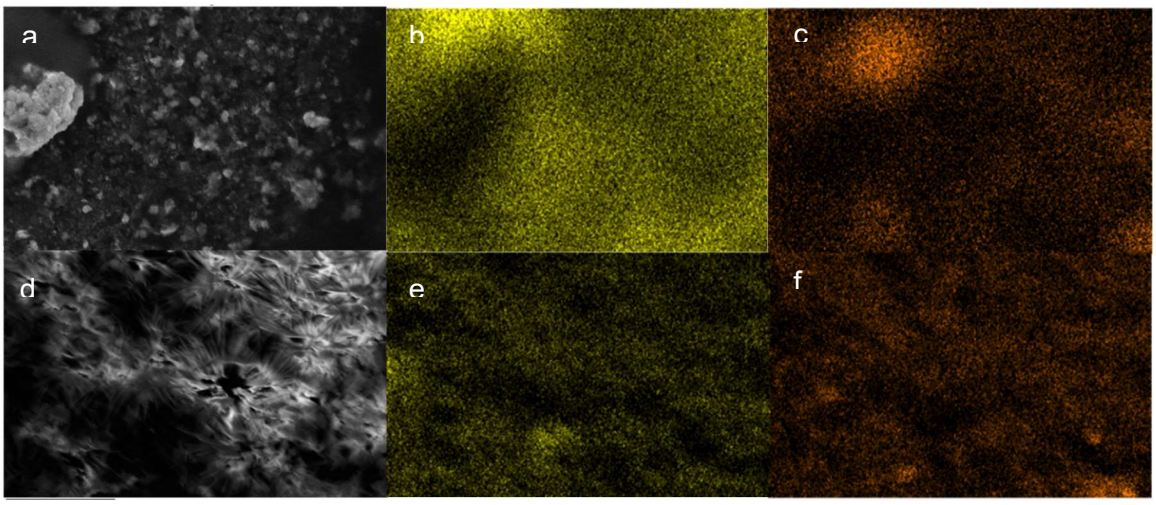


**Figure S8:** SEM image (a) and elemental mapping of Cu (b) and C (c) before electrolysis. After electrolysis (30 min at -0.98V vs. RHE) an equivalent SEM image (d) and Cu (e) and C (f) elemental mapping was acquired for Cu catalysts.

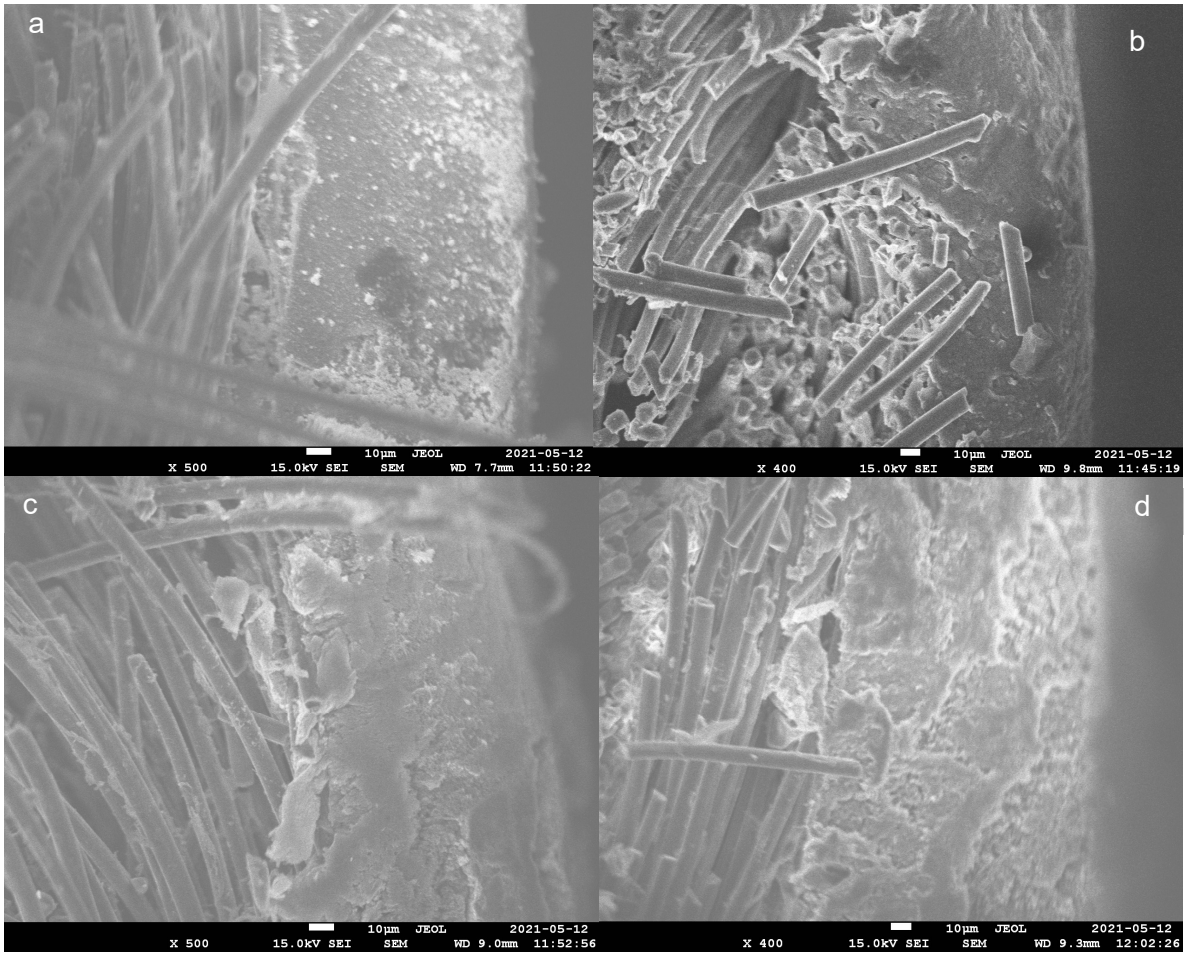


**Figure S9:** SEM images of the cross session (a) CuO/C before reaction; (b) CuO/C after reaction; (c) Cu/C before reaction; (d) Cu/C after reaction.

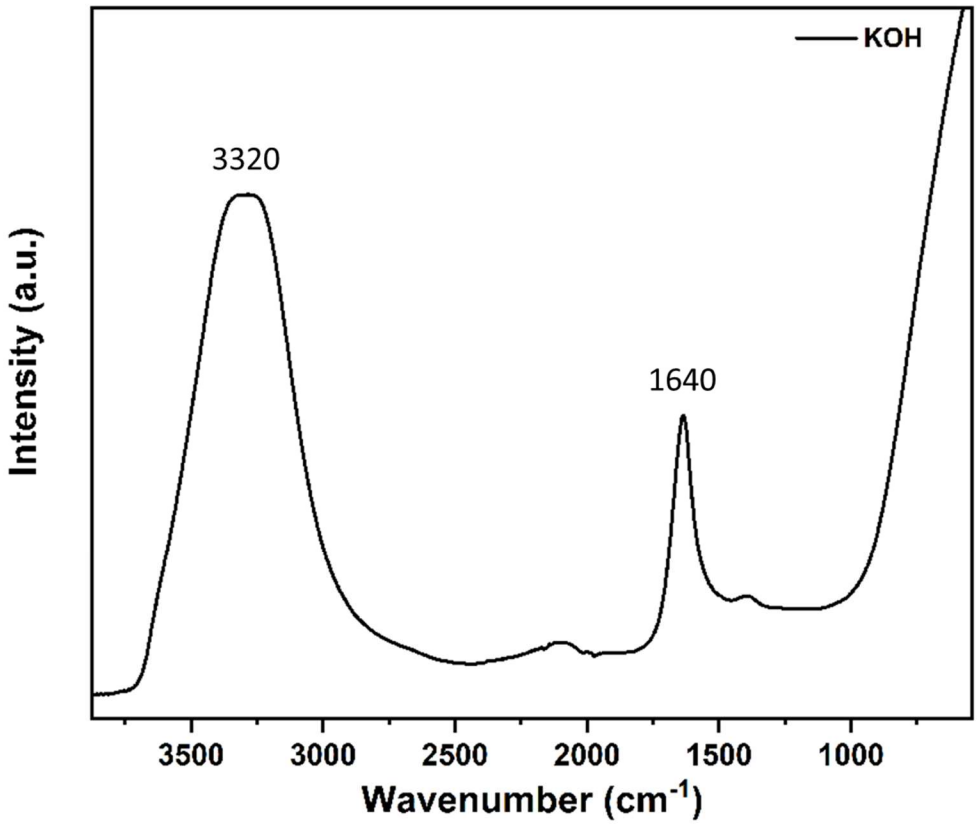


**Figure S10:** IR spectrum of 1M KOH

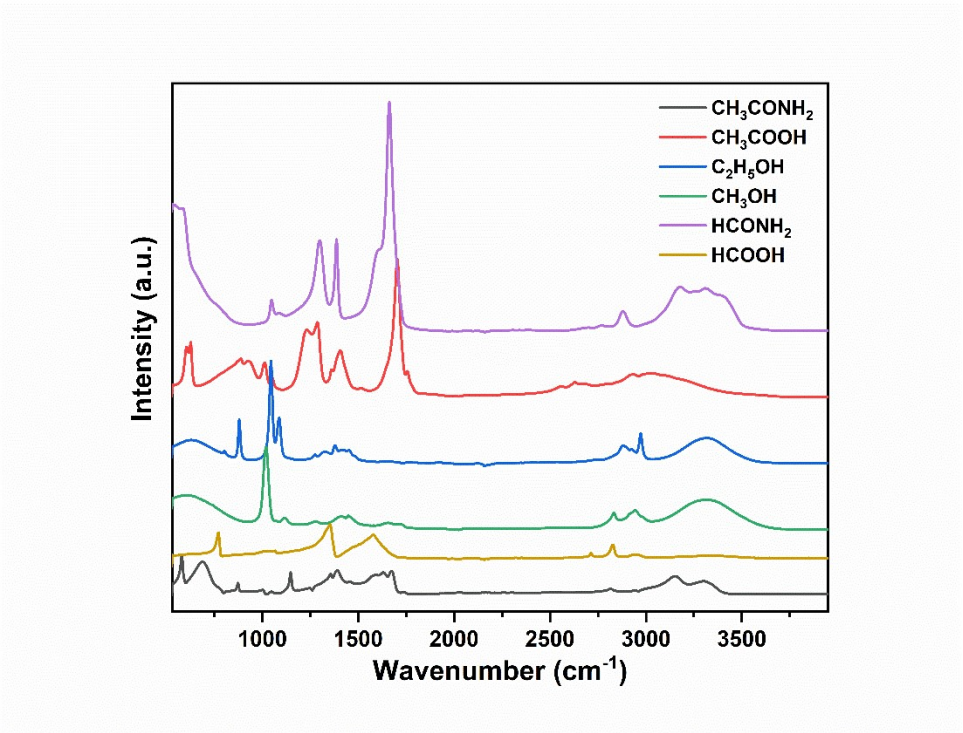


**Figure S11:** IR spectra of several products detected in $NH_3$ + $CO_2$ electrolysis

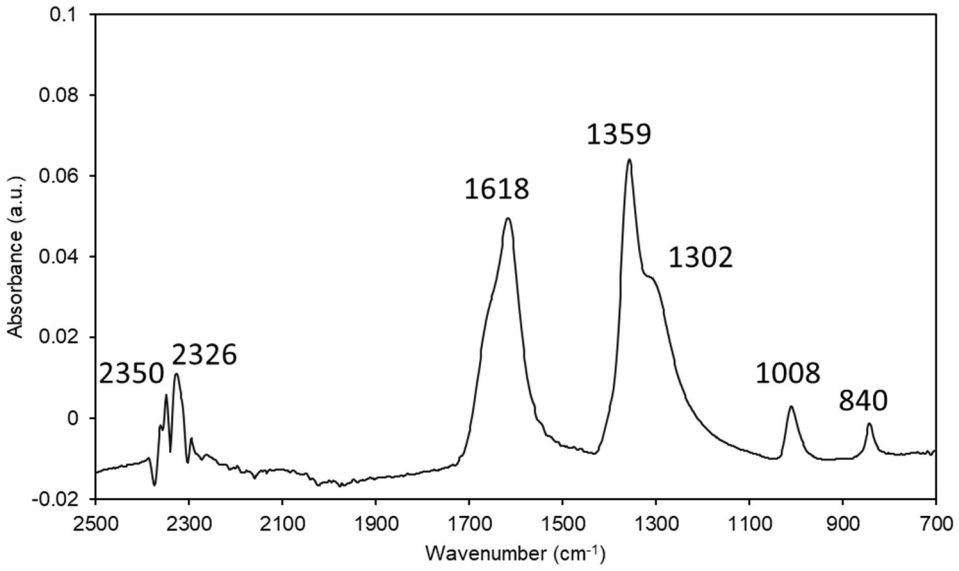


**Figure S12:** IR spectrum of the spectroelectrochemical setup with a $CO_2$ flow in 1M KOH, using an Ar flow in 1M KOH as the background. Peaks attributable to $CO_2$ and carbonate are present.

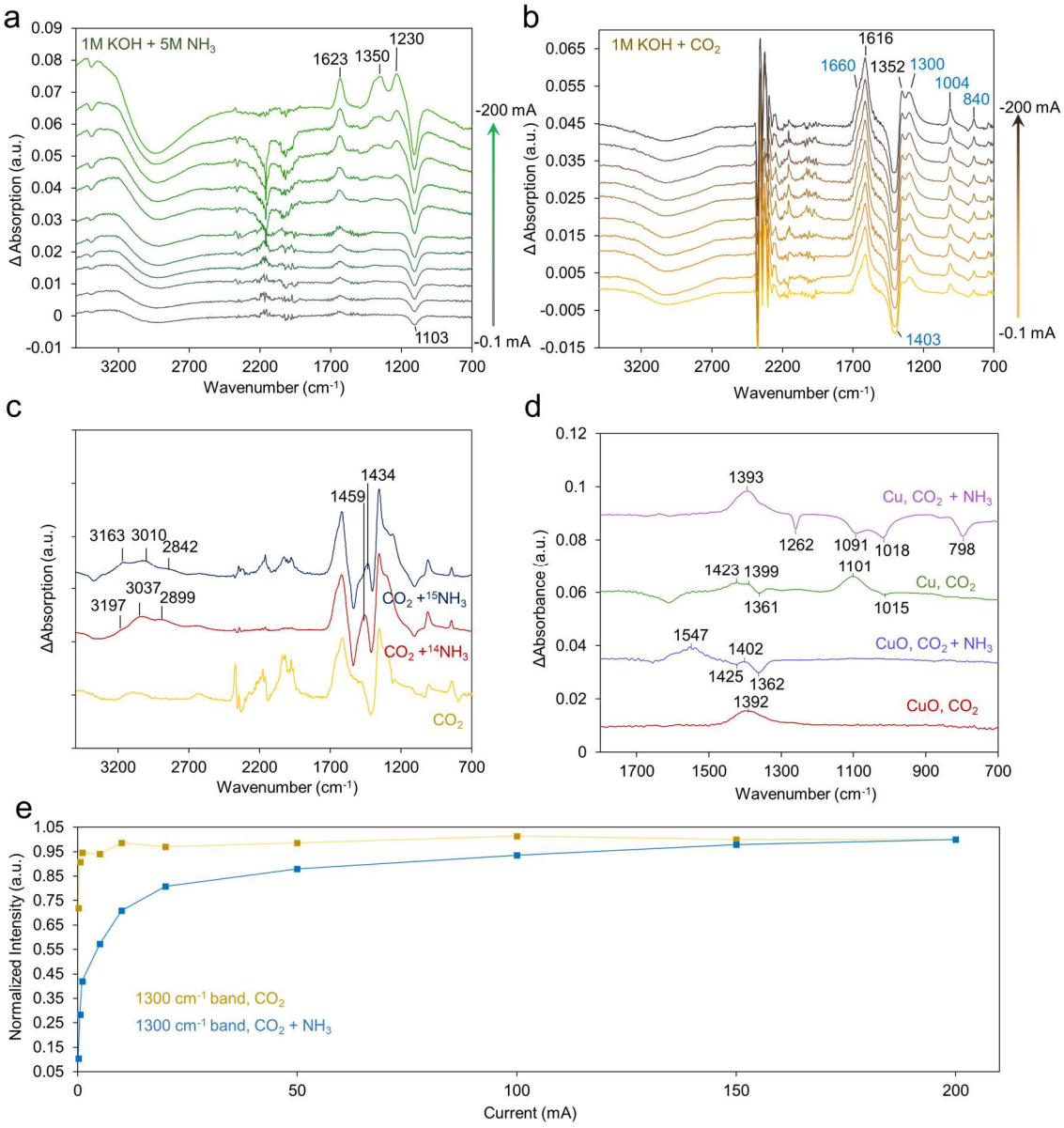


**Figure S13:** With the system as open circuit used as the background, spectra were acquired at select operating currents in the presence of $NH_3$ only (a) and $CO_2$ only (b). With $CO_2$ and $^{15}NH_3$ reactants, the spectra in (c) are used to identify the peaks belonging to $^{15}NH_4^+$ as it forms during reaction conditions. Subtracting out the (bi)carbonate contributions helps see weaker bands from intermediates (d). The rise of the bicarbonate peak, normalized to itself at 200 mA, is relatively slower with $NH_3$ present, indicating a slower generation of this species.

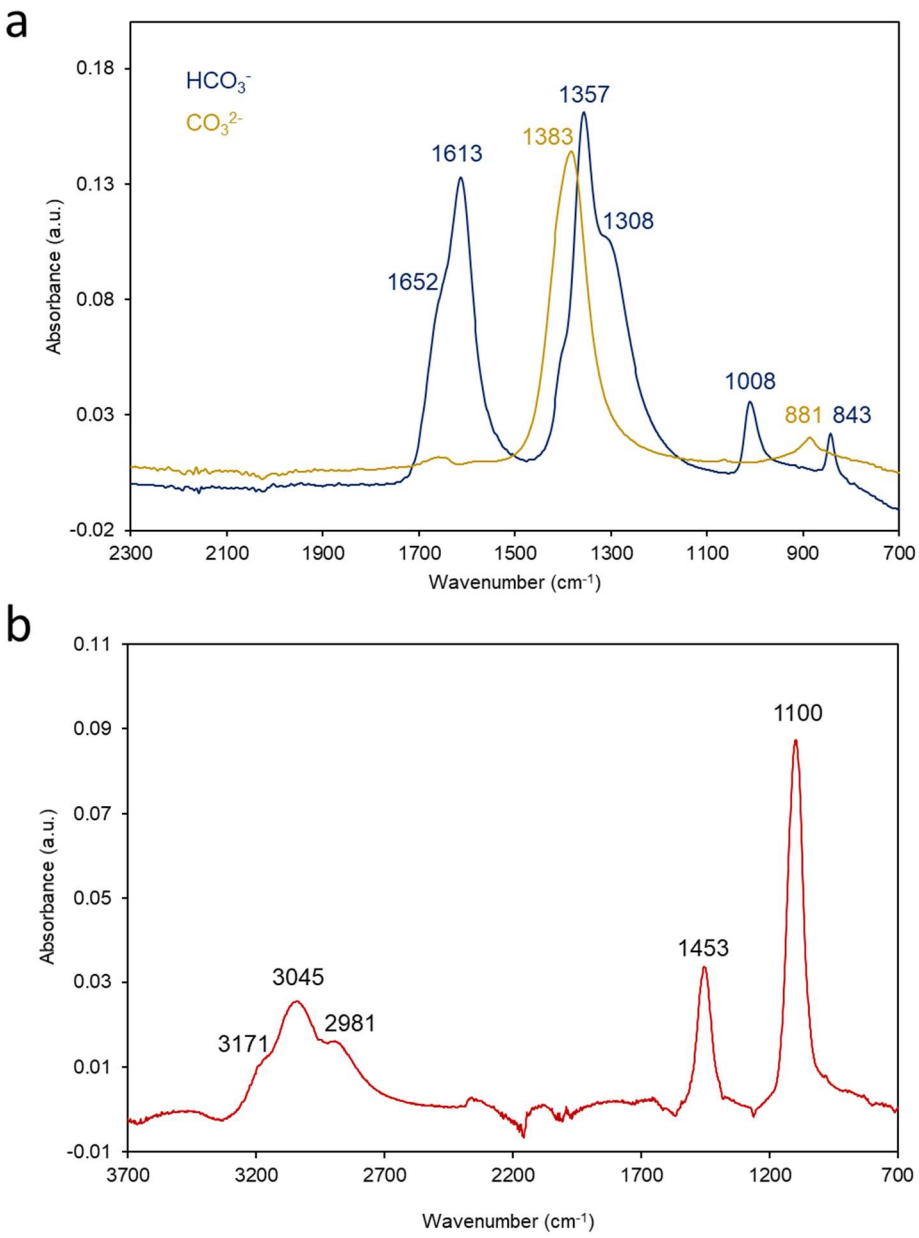


**Figure S14:** IR spectra of $KHCO_3$ and $K_2CO_3$ dissolved in water (a) and $NH_4^+$ (b)

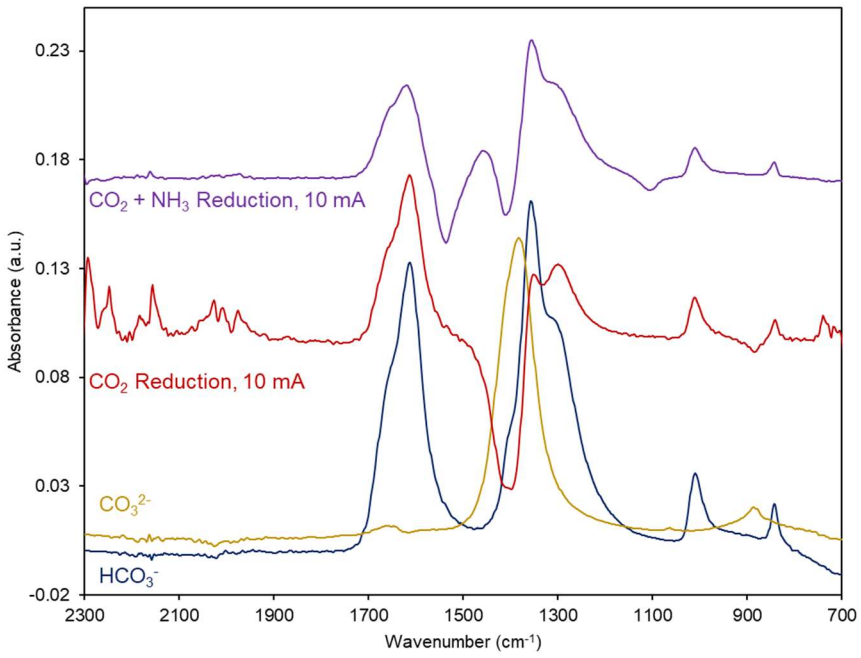


**Figure S15:** Overlaid spectra of (bi)carbonate and $CO_2$ reduction

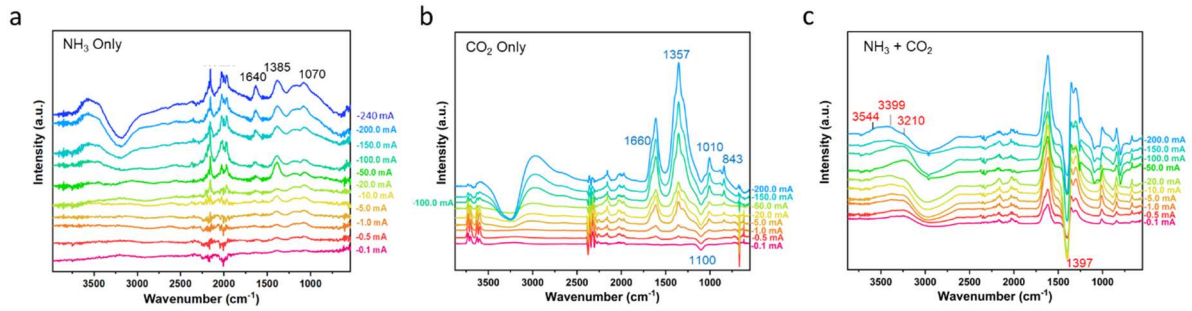


**Figure S16:** IR spectra of Cu catalysts, with $NH_3$ only (a), $CO_2$ only (b), and $NH_3$ + $CO_2$ (c).

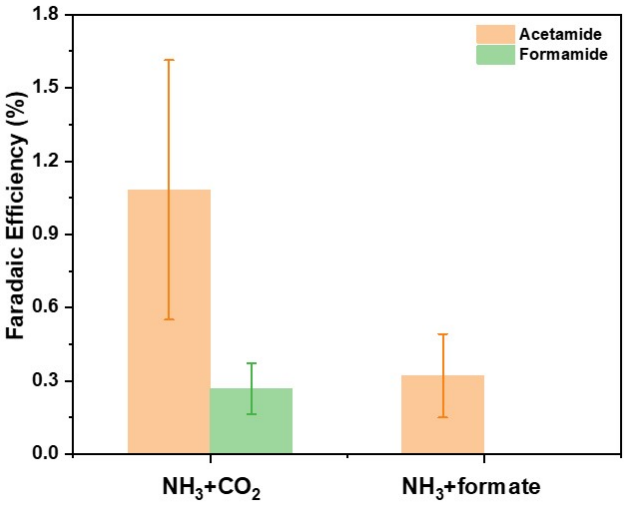


**Figure S17:** C-N bond formation using 150 mM NaCOOH as the C-source instead of $CO_2$ in otherwise identical conditions (1M KOH, -0.98V vs. RHE, Cu catalyst). The average partial current for acetamide in the formate case was 0.2 mA/cm$^2$.

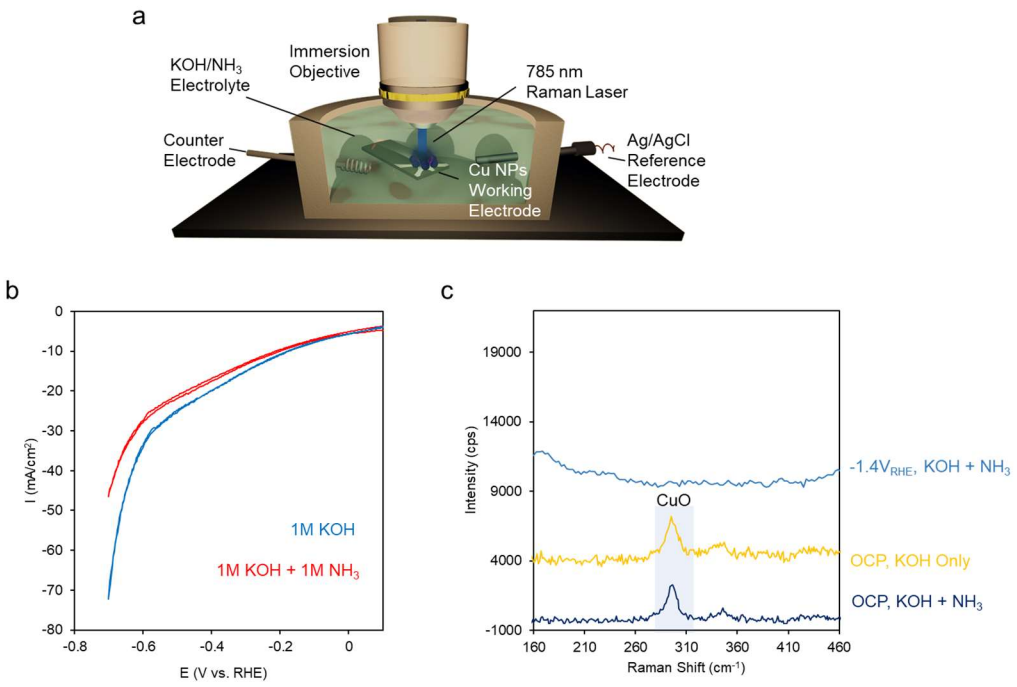


**Figure S18:** The addition of $NH_3$ to the electrolyte suppressed the water reduction current of Cu nanoparticles (a). Surface-enhanced Raman revealed the reduction of the surface oxide under a negative bias of -1.4V vs. RHE but no new bands that could be assigned to Cu-N species (a). Therefore, we believe that the $NH_3$ is near the electrode surface and alters the catalysis of the Cu without directly binding to it. Further, the decrease of current indicates that likely the $NH_3$ does not act as a proton donor for hydrogen evolution at rates higher than that of water.

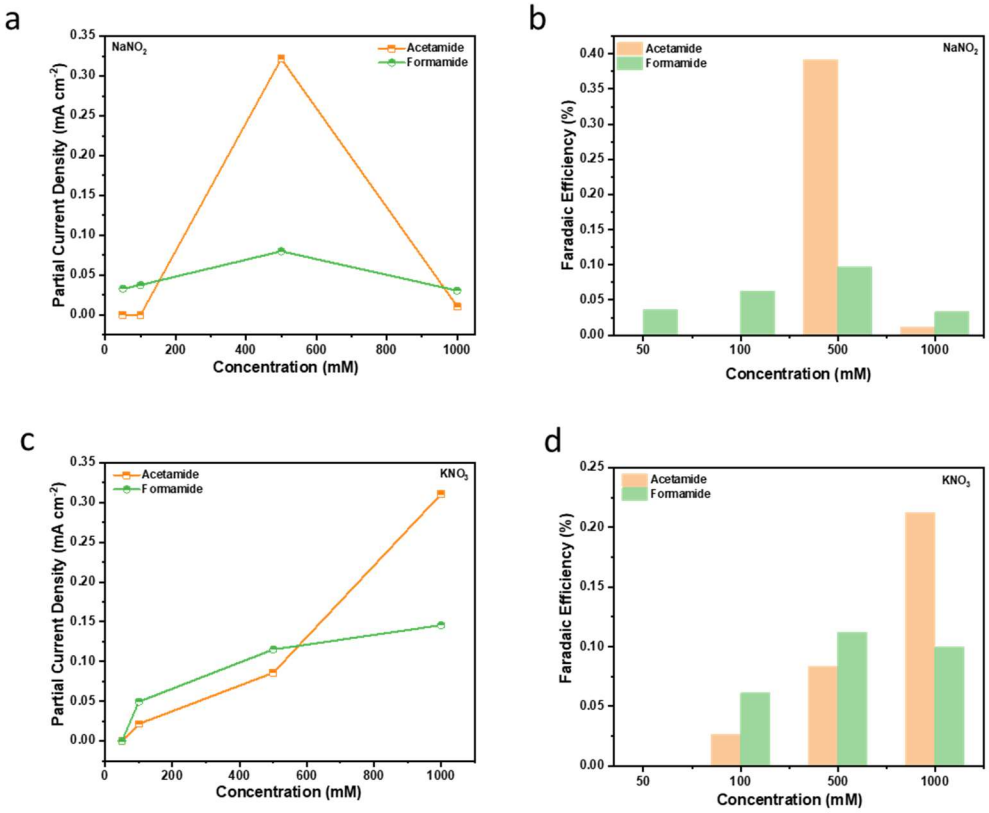


**Figure S19:** Partial current density (a) and Faradaic efficiency (b) for C-N products from $NaNO_2$ with Cu catalysts at -0.98V vs. RHE) as a function of reactant concentration in the liquid phase. Similarly, we measured the partial current density (a) and Faradaic efficiency (b) for C-N products from $KNO_3$ with Cu catalysts at -0.98V vs. RHE).

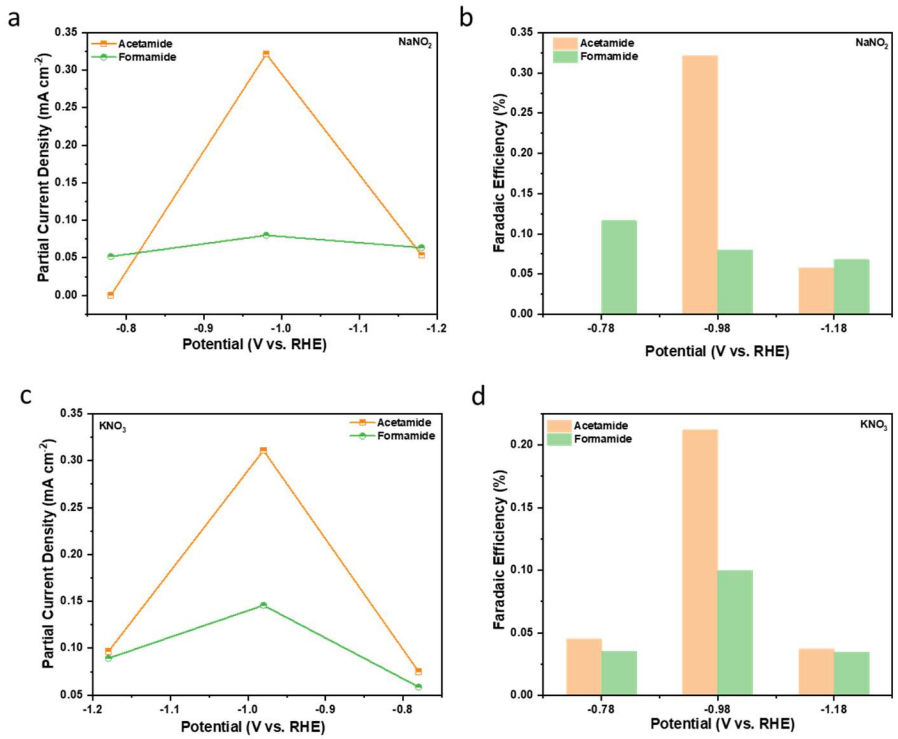


**Figure S20:** Partial current density (a) and Faradaic efficiency (b) for C-N products from $NaNO_2$ with Cu catalysts at -0.98V vs. RHE) as a function of potential. Further, we measured the partial current density (a) and Faradaic efficiency (b) for C-N products from $KNO_3$ with Cu catalysts at the above optimized concentration.

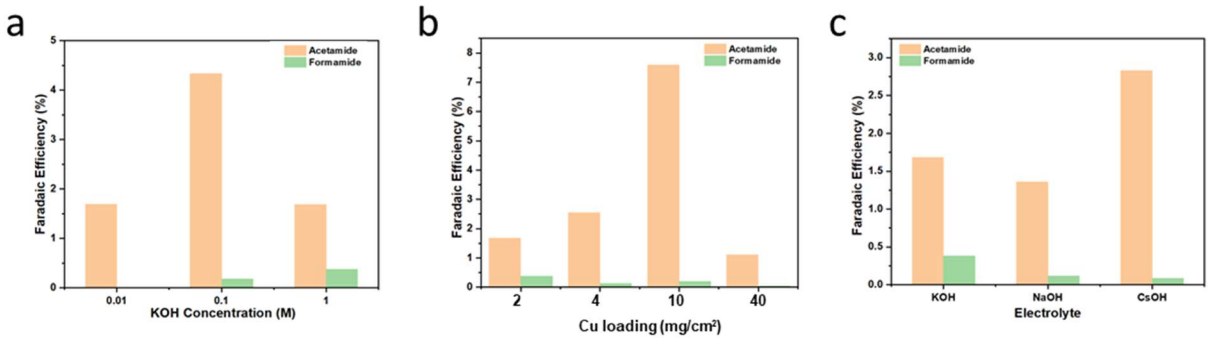


**Figure S21:** Optimization of reaction conditions with (a) different concentrations of KOH; (b) different amount of Cu nanoparticles; (c) electrolyte (1M) with different cations. The applied potential was -0.98V vs. RHE for this round of experiments.

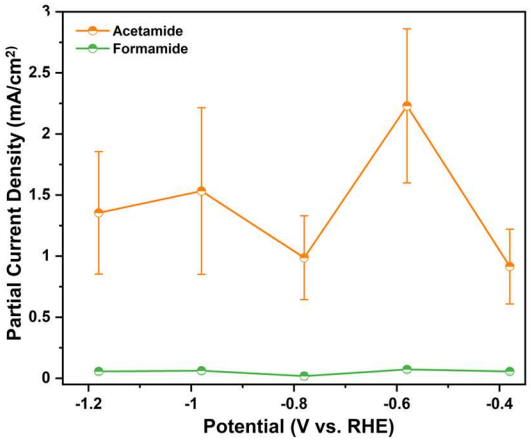


**Figure S22:** Partial current density for acetamide and formamide corresponding to the Faradaic efficiency at each potential in figure 6 in the main text.

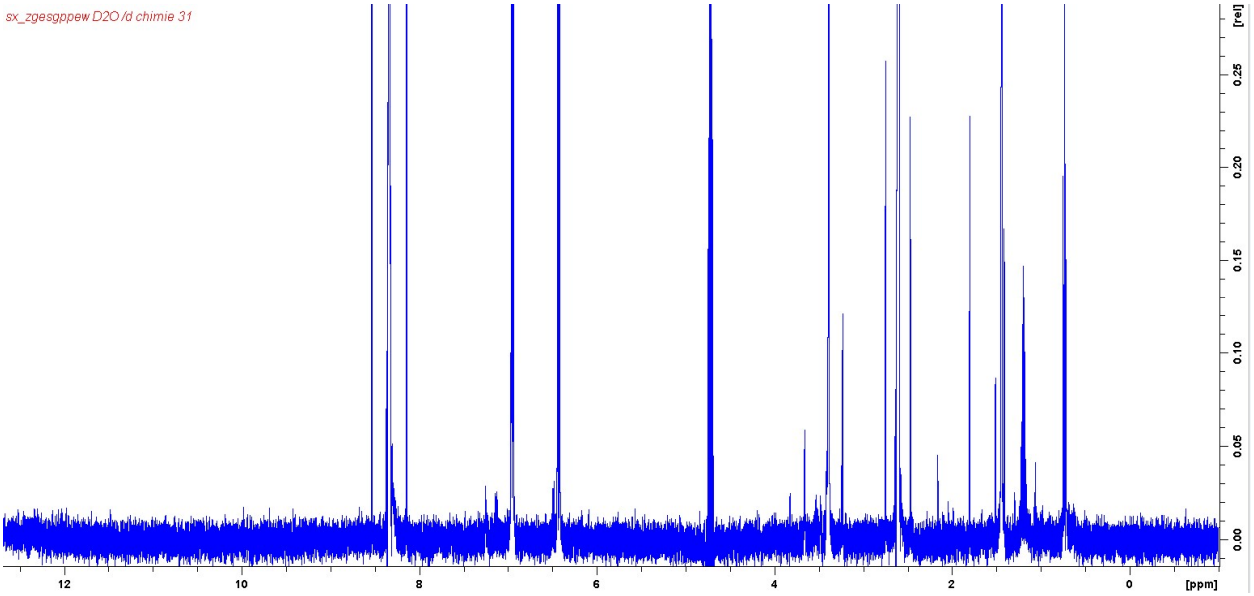


**Figure S23:** NMR spectrum under open circuit potential. 50 mM formate was added to 1M $NH_3$ + 1M KOH for 1 hour and the solution probed afterwards. No formamide or acetamide could be detected.

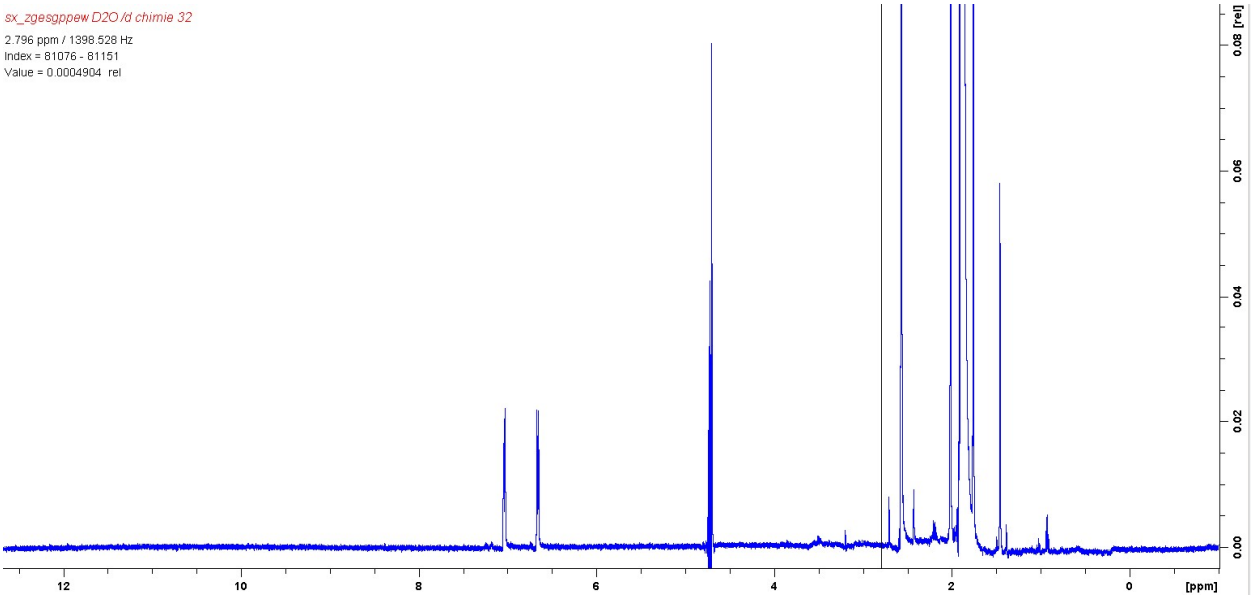


**Figure S24:** NMR spectrum under open circuit potential. 50 mM acetate was added to 1M $NH_3$ + 1M KOH for 1 hour and the solution probed afterwards. No formamide or acetamide could be detected.